ARTICLE   **Open Access**

Super-assembled compressible carbon frameworks featuring enriched heteroatom defect sites for flexible Zn–air batteries

Huaipeng Pang[1], Meng Wang[1], Peipei Sun[1], Wenshuai Zhang[1], Dan Wang[1], Runhao Zhang[1,2], Li Qiao[1], Weijie Wang[1], Meng Gao[1], Yong Li[1], Jiang Chen[3], Kang Liang[4] and Biao Kong[2,5]

Abstract

Flexible Zn–air batteries (FZABs) exhibit low cost and inherent safety and have potential for application in wearable electronic devices. Nevertheless, balancing the high energy density and flexibility of the self-supported electrodes in FZABs is still a challenge. Herein, we develop a novel superassembly strategy for the preparation of N, S-codoped porous carbon frameworks (NS@CFs) as cathodes in FZABs. Benefiting from the abundant heteroatom defect sites, NS@CF exhibits excellent electrocatalytic performance for the oxygen reduction reaction (ORR), including high electrochemical activity and long-term stability. When used as the cathode in a liquid flowing ZAB, NS@CF exhibited a power density of 221 mW cm^{-2} and achieved a 60% improvement over Pt/C-based ZABs. This new ZAB exhibited a high specific capacity of 792 mA h g$_{Zn}^{-1}$, excellent long-term durability and cycling stability, which is superior to those of ZABs assembled with commercial Pt/C cathodes. In addition, the flexible NS@CF with directional channels can be used as independent air cathodes for FZABs, where it provides small charge/discharge voltage gaps, a power density of 49 mW cm^{-2} and outstanding cycling stability. This work provides a novel strategy for designing and fabricating highly efficient integrated electrodes for flexible and wearable electrochemical devices.

Introduction

The rapid advancement with wearable and portable electronic devices urgently requires the development of flexible and safe batteries[1–3]. Among the different classes of batteries, Zn–air batteries (ZABs) have been widely studied due to their high theoretical energy densities and inherent advantages of safety, environmental friendliness and low cost[4,5]. Based on the slow kinetics of the ORR, air electrode catalysts are key to the high performance of ZABs. Recently, catalysts including noble metals, nonprecious metal oxides and heteroatom-doped carbon nanomaterials have been reported[6–8]. It has been common to make slurries of these powdered catalysts and then apply them to flexible conductive substrates, such as carbon cloth and metal foil, by spraying, coating, or drop coating methods[2,5]. However, these powder catalysts are often prone to poor air/electrolyte permeability and inefficient air diffusion due to their overly dense structures and thus fail to achieve the desired electrochemical performance[9,10]. Currently, research attention is focused on direct syntheses of integrated electrodes without the use of additives such as binders or conductive agents, for example, with carbon-based films obtained via the electrostatic spinning technique and carbon cloth treated by electrodeposition or in situ growth[11,12].

The role of the ORR in discharging and charging of rechargeable ZABs has been well studied, but the sluggish reaction kinetics of the ORR lead to large overpotentials,

Correspondence: Meng Wang (wangmeng@sdas.org) or
Biao Kong (bkong@fudan.edu.cn)
[1]National Supercomputer Research Center of Advanced Materials, Advanced Materials Institute, Qilu University of Technology (Shandong Academy of Sciences), Jinan 250014, P. R. China
[2]Department of Chemistry, Shanghai Key Lab of Molecular Catalysis and Innovative Materials iChEM, Fudan University, Shanghai 200433, P. R. China
Full list of author information is available at the end of the article
These authors contributed equally: Huaipeng Pang, Meng Wang

low energy efficiencies, and poor power densities, which remain a great challenge[13]. Today, platinum (Pt) oxides and ruthenium (Ru) are usually considered standard catalysts. However, the high cost, scarcity, and poor stability of these noble metal-based catalysts hinder practical application in rechargeable ZABs[14]. Previous studies have demonstrated that heteroatom-doped carbon nanomaterials serve effectively as ORR catalysts, and some of them even outperform noble metal catalysts[14,15]. Extensive studies have shown that N and S have electronic structures and atomic radii similar to those of C, and they also have different electronegativities and electron affinities; this leads to charge redistribution and spin state changes in sp^2 carbon planes when the catalysts enter carbon nanomaterials, which promotes adsorption of oxygen and its intermediates on the catalyst and facilitates electron transport in oxygen reactions[16].

Cellulose nanofibers (CNFs) have received much attention as renewable and environmentally friendly nanomaterials, and they possess the basic characteristics of cellulose and the typical characteristics of nanomaterials, such as light mass, high surface activity, strong adsorption capacity, and high reactivity[17]. A CNF carbon framework (CF) composed of an ultralight interconnected and monolithic framework with a graded porous structure is an excellent electrocatalyst due to its fluffy and porous structure, which facilitates the air-electrolyte-catalyst catalytic reaction and offers more active sites[18]. However, high-temperature annealing of CNFs usually produces more amorphous carbon and results in a fragile and weak structure for the CF, which makes it difficult to meet the mechanical flexibility requirements of FZABs[19]. Thus far, achieving carbon frameworks with both high flexibility and high electrocatalytic performance is still a challenge.

Herein, we developed a novel fabrication strategy using CNFs and carbon nanotubes (CNTs) prepared via interfacial superassembly[20–22] to construct flexible carbon framework electrocatalysts for self-supported flexible air electrodes. The obtained NS@CF had a directional porous structure, and the heteroatoms were uniformly doped in the carbon framework, which resulted in abundant active sites, excellent mechanical flexibility, and ORR electrocatalytic activity. Flexible carbon frameworks have important research significance as novel electrode materials and enable innovative development of flexible energy storage devices.

Results and discussion

Preparation of the N, S-codoped porous carbon frameworks is shown in Fig. 1. CNFs possess abundant oxygen-rich groups (-OH and -COOH), which are
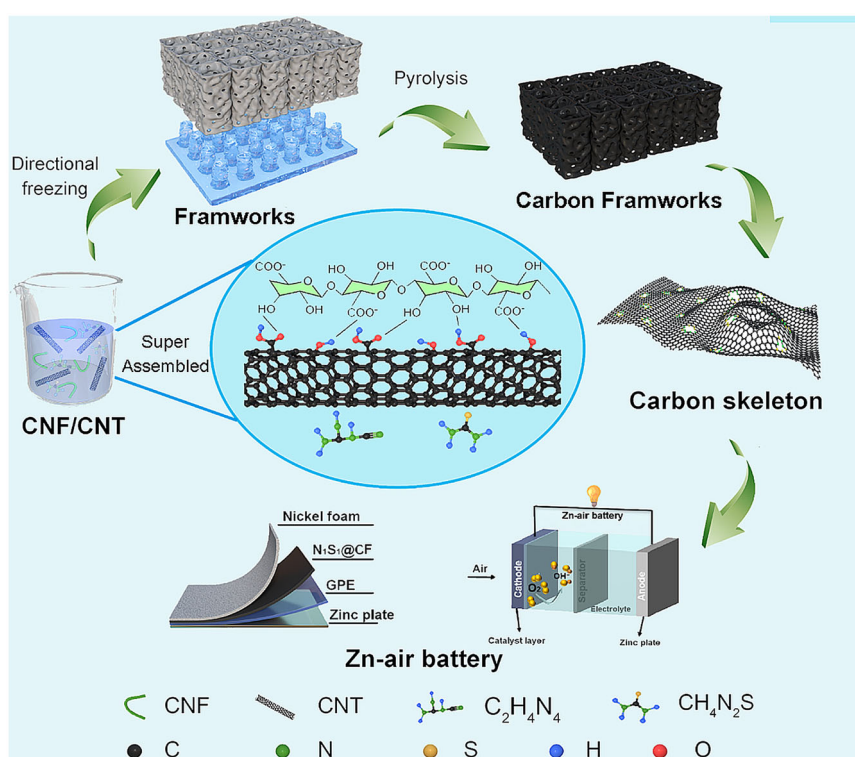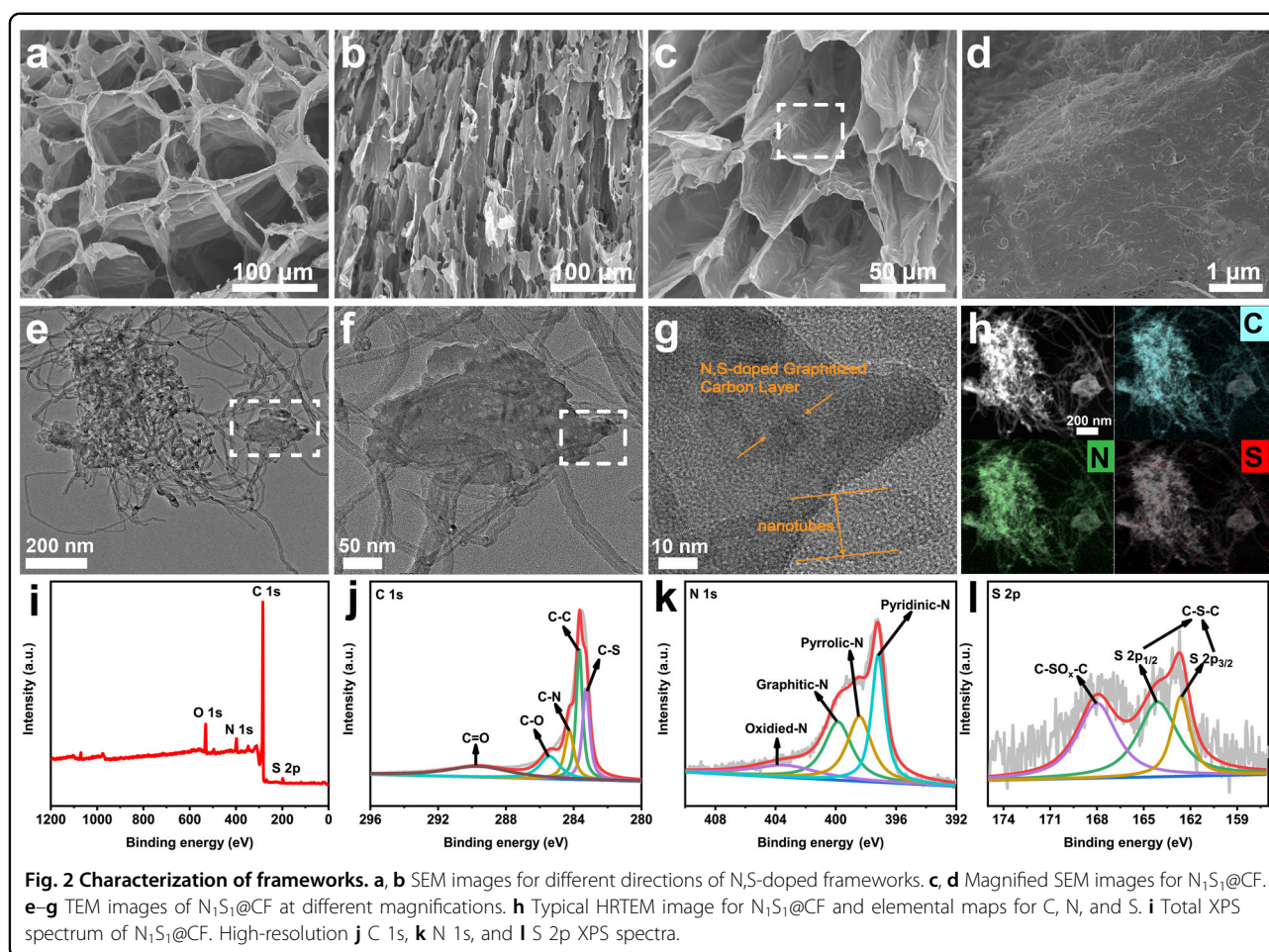

Fig. 1 The synthesis process of N₁S₁@CF. The schematic showed the CNF/CNT mixture is firstly assembled by H-bonds. Then the carbon framwork is fabricated by freeze-drying and pyrolysis, which can be used in FZABs.

Fig. 2 Characterization of frameworks. a, **b** SEM images for different directions of N,S-doped frameworks. **c**, **d** Magnified SEM images for N_1S_1@CF. **e**–**g** TEM images of N_1S_1@CF at different magnifications. **h** Typical HRTEM image for N_1S_1@CF and elemental maps for C, N, and S. **i** Total XPS spectrum of N_1S_1@CF. High-resolution **j** C 1s, **k** N 1s, and **l** S 2p XPS spectra.

particularly important in preventing aggregation of the CNTs because of their strong negative surface charges, as indicated in Figs. S1 and S2. This enables sufficiently homogeneous dispersion of CNFs and CNTs in water and confers the unique advantages of high flexibility and integrity on the prepared monolithic frameworks[16]. Dicyandiamide and thiourea were used as small molecule precursors for nitrogen and sulfur and were uniformly dispersed with CNFs and CNTs in the mixed solution. In the process of directional freezing, the vertical temperature difference induced an ice crystal to grow vertically along the bottom and to form a columnar ice crystal structure. After the ice crystals were removed by freeze-drying, an oriented porous framework structure was formed. Moreover, the pyrolysis process eventually led to interfacial assembly of N and S in the carbon framework. It is noteworthy that the introduction of reactive carbon substrates via N and S atom doping was accompanied by creation of various defects and porous structures on a micro/macro scale[17]. For this purpose, N, S-codoped CNF/CNT carbon frameworks with flexibility and electrochemical activity were obtained after freeze-drying and high-temperature pyrolysis, and they can be used with FZABs.

The scanning electron microscopy (SEM) image in Fig. 2a shows that the CNF/CNT frameworks were composed of interconnected porous carbon nanosheets. These large pores were formed due to sublimation of the ice crystals during freeze-drying. The SEM image for the CNF/CNT frameworks in the horizontal direction, as shown in Fig. 2b, further revealed a directional porous structure. After pyrolysis, this directional porous structure was retained in the carbon frameworks (Fig. 2c). Similar structures were observed in the control samples N_1S_2@CF and N_2S_1@CF with different ratios (Fig. S3). This directional porous structure provided a large number of active sites and a large contact area between the catalyst and the electrolyte to enhance the electrocatalytic performance[18]. As indicated in Fig. 2d, the CNTs were uniformly dispersed in the carbon framework, which was used as an enhanced skeleton for the NS@CF.

As demonstrated in Fig. S4, the volume of the carbon framework shrank after pyrolysis, which was ascribed to the dehydration, decarboxylation, and decarbonylation
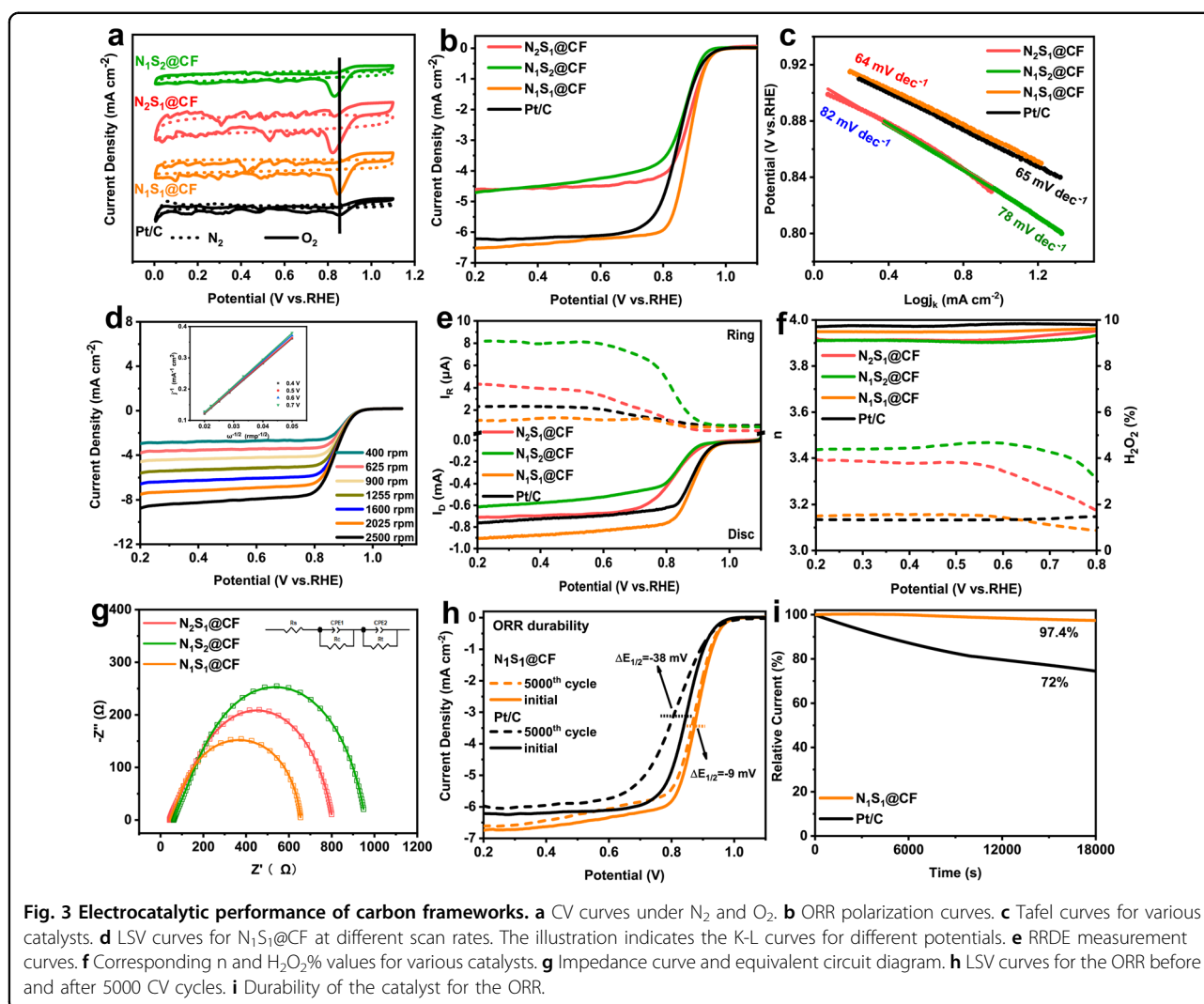
reactions of cellulose[19]. The N_1S_1@CF had a low density of 4.17 mg cm^{-3} and could stand on soft grass without any damage. Moreover, N_1S_1@CF displayed high compressibility and fatigue resistance. As shown in Figs. S5a and S6a, N_1S_1@CF withstood a wide range of compressive strains ranging over 0–90% due to the ordered porous directional structure. The loading stress−strain curves can be divided into two regions, including the initial linear elastic region (strain ≤ 70%) under a low stress of 19 kPa, which corresponds to the oriented arrangement of the pores, and the following densifying region (strain ≥ 70%) exhibiting a rapid increase in stress, which indicated densification of the framework skeleton[20]. As indicated in Figs. S5b and S6b, the system retained 88% of its maximum stress after 100 cycles without plastic deformation at 50% compressive strain, which revealed its excellent fatigue resistance. More impressively, N_1S_1@CF exhibited a high retention rate of 94% even at a high strain of 90%, demonstrating excellent compressibility and elasticity[21].

Transmission electron microscopy (TEM) images are shown in Fig. 2, f. Cellulose carbon fibers and CNTs were closely connected to each other, which resulted in a robust carbon skeleton. In the high-resolution TEM (HRTEM) image (Fig. 2g), distinct nanotube-graphitized carbon layers as well as N, S-codoped graphitized carbon layers were evident, which indicated that the CNFs and CNTs were connected and highly graphitized. The corresponding elemental maps in Fig. 2h further verified the uniform distributions of N and S on the carbon skeleton and carbon nanotubes. In the X-ray diffraction (XRD) patterns for CF and N_1S_1@CF (Fig. S7), only two sharp diffraction peaks at approximately 25.6° and 43.5° were observed, which corresponded to the C (002) and (100) planes, respectively, and there were no obvious impurity peaks, indicating that the series mainly comprised carbon materials[22]. It is noteworthy that the diffraction intensity became larger and the peak position shifted to the right after N and S doping, which on the one hand indicated successful doping of nitrogen and sulfur into the carbon framework; on the other hand, it proved that upon heteroatom doping, the higher electronegativities of nitrogen and sulfur relative to that of carbon resulted in deformations of the crystalline structure, an increase in active sites, and formation of disordered crystalline carbon[23]. In addition, the carbon components were further distinguished by Raman spectroscopy. As shown in Fig. S8, the peak for the graphite layer (G band) was at approximately 1580 cm^{-1}, and the peak for disordered carbon (D band) was at approximately 1360 cm^{-1}. The intensity ratio (I_D/I_G) of the D and G bands provides information on the presence of abundant defects and the degree of graphitization in the graphitic carbon matrix. The Raman spectrum of N_1S_1@CF had a higher I_D/I_G (1.03) than other samples due to the presence of abundant defects. In

addition, N and S atoms saved considerable space without destroying the highly graphitized framework, and defects were introduced into N_1S_1@CF. A matrix with a high degree of graphitization and ample defect sites is expected to show improved electron transfer efficiency and electrocatalytic activity[24].

The porosities of the carbon frameworks were determined with Brunauer–Emmett–Teller (BET) N_2 adsorption measurements. As indicated in Fig. S9a, all samples displayed type IV isotherms, indicating the presence of mesopores and fewer micropores[23]. By comparison, N_1S_1@CF had the largest specific surface area (144.36 m^2 g^{-1}), which is essential for high electrocatalytic activity of the material. However, only the surfaces that are easily accessible to reactants are truly useful, and utilization of the surface area is largely determined by the pore structure of the material. Fig. S9b and Table S1 show that N_1S_1@CF had an average pore size of 15 nm, confirming its mesoporosity. The large specific surface area and pore size are conducive to full utilization of active sites and effective mass transfer, which are beneficial for improvement of electrocatalytic performance[25].

From current research progress, it is known that the key factor affecting catalytic activity is the type of bonding established between the doped heteroatoms and carbon atoms. The distribution of each element and the bonding among elements in N_1S_1@CF were examined by X-ray photoelectron spectroscopy (XPS). As indicated in Fig. 2i and Table S2, the complete XPS spectrum clearly showed four peaks and atomic percentages for C, N, S, and O elements. The peaks in the C 1s, N 1s, and S 2p XPS spectra were deconvoluted to clarify the bonding type for each atom. As demonstrated in Fig. 2j, the peaks at 285.8 eV, 284.7 eV, and 283.4 eV in the C 1s spectrum corresponded to C−N, C−C, and C−S, respectively, which demonstrated that N and S were successfully doped into N_1S_1@CF, while the other, weaker peaks were attributed to C−O and C=O species. The high-resolution asymmetric N 1s spectrum for N_1S_1@CF showed peaks at 397.2 eV, 398.5 eV, 400.1 eV, and 403.4 eV, which corresponded to pyridine-N, pyrrole-N, graphite-N, and oxide-N moieties, respectively. Figures 2k and S10 show that the contents of pyridinic N and graphite-N were higher than those of the others. On the one hand, pyridine-N had a stronger electron-attracting ability; on the other hand, graphite-N changed the morphology of the carbon, which is beneficial for the electrochemical process of N_1S_1@CF[26]. As indicated in Fig. 2l, the three peaks in the high-resolution S 2p spectrum of N_1S_1@CF were at 162.6 eV, 164 eV, and 168.1 eV and corresponded to C=S−C, C−S−C, and C−Sox−C bonds, respectively. In addition, the C−S−C and C=S−C bonds indicated that S atoms were mainly present in the form of thiophene sulfur; this led to disordered stacking of the lamellar

Fig. 3 Electrocatalytic performance of carbon frameworks. a CV curves under N_2 and O_2. **b** ORR polarization curves. **c** Tafel curves for various catalysts. **d** LSV curves for $N_1S_1@CF$ at different scan rates. The illustration indicates the K-L curves for different potentials. **e** RRDE measurement curves. **f** Corresponding n and $H_2O_2\%$ values for various catalysts. **g** Impedance curve and equivalent circuit diagram. **h** LSV curves for the ORR before and after 5000 CV cycles. **i** Durability of the catalyst for the ORR.

structure, and the five-membered ring structure of thiophene exposed more active sites in the structures of the carbon-based material lamellae. It has been confirmed that pyridine nitrogen, graphite-N, and thiophene-S have strong relationships with catalytically active ORR sites[27]. N atoms effectively increase the electrical conductivity of the carbon material, and S atoms expand the spacings between carbon layers, thus improving charge mobility and accessibility of active species. Hence, the higher pyridine-N and thiophene-S contents in $N_1S_1@CF$ are expected to help improve its oxygen reduction performance[28].

To understand the electrocatalytic performance of the samples, we evaluated the ORR electrocatalytic activity of $N_1S_1@CF$ in alkaline solution with a rotating disc electrode (RDE) test and used commercial Pt/C (20 wt%) as a benchmark. Figure 3a displays the cyclic voltammetry (CV) curves for the prepared materials in N_2- and O_2-saturated 0.1 M KOH solutions, respectively, and a
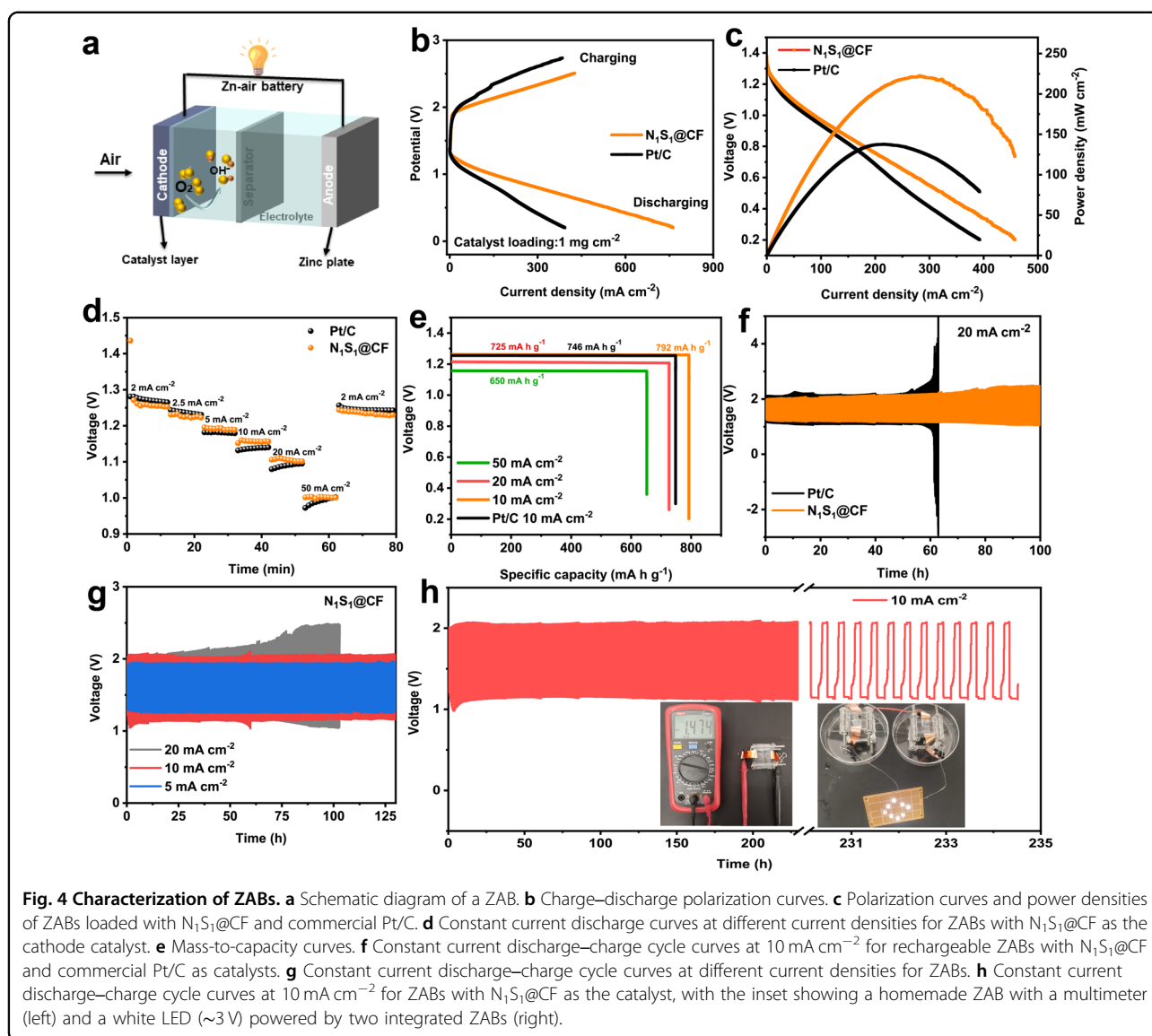
distinct oxygen reduction peak was observed in the CV curve for O_2. As the doping ratio was changed, the reduction peak became increasingly pronounced and gradually shifted to a positive potential, indicating increased ORR activity. Figure 3b shows linear sweep voltammetry (LSV) comparison curves generated at 1600 rpm and with 0.1 M KOH for all samples, which indicated that the onset potentials (E_{onset}), half-wave potentials ($E_{1/2}$), and limiting current densities (J_L) of $N_1S_1@CF$ were 0.98 V, 0.88 V, and 6.52 mA cm^{-2}, respectively. All of these properties were equivalent to or better than those of standard Pt/C catalysts (0.98 V for E_{onset}, 0.85 V for $E_{1/2}$, and 6.2 mA cm^{-2} for J_L). These results indicated that the $N_1S_1@CF$ catalyst had higher ORR catalytic activity in alkaline solution (Table S3). Moreover, the catalytic properties of $N_1S_1@CF$ were tested over 100 compression cycles at 50% strain. As shown in Fig. S11, the ORR properties of $N_1S_1@CF$ were almost unchanged. In addition, we evaluated the kinetic

performance of the catalysts by calculating the Tafel slopes from ORR polarization curves of the catalysts. The slopes of the Tafel curves for $N_1S_1@CF$, $N_1S_2@CF$, $N_2S_1@CF$, and commercial Pt/C are shown in Fig. 3c and were 64, 82, 78, and 65 mV dec^{-1}, respectively. $N_1S_1@CF$ exhibited a relatively low Tafel curve slope, indicating that it is an excellent ORR catalyst with fast kinetics similar to those of commercial Pt/C[29]. Then, as demonstrated in Fig. 3d, the RDE was subjected to LSV tests at different rotational speeds, and different polarization curves were obtained; then the Koutecky-Levich (K-L) equation was used to obtain the number of electrons transferred by $N_1S_1@CF$ during the catalytic ORR reaction (Fig. 3d inset). The K-L curves were generated at four voltages, the number of electrons transferred was calculated and then averaged, and the result was 3.89, which was close to 4. This indicated that the ORR reaction catalyzed by $N_1S_1@CF$ proceeded via a four-electron transfer path, and $N_1S_1@CF$ had excellent electrocatalytic activity[30]. In addition, to investigate the ORR reactions of the synthesized catalysts, rotating ring disc electrode (RRDE) measurements were also performed, as indicated in Fig. 3e. We calculated the number of electrons transferred (n) and the H_2O_2% from the corresponding disk current and ring current, and Fig. 3f shows that the number of electrons transferred was closer to 4 and fewer intermediates were generated by the materials higher catalytic activities; this was similar to the behavior of Pt/C and constituted general agreement with the number of transferred electrons determined from the slope of the K-L equation. In summary, the ORR in $N_1S_1@CF$ was closer to the four-electron fast kinetic reaction process[31]. To gain insight into the ORR behavior of $N_1S_1@CF$ in alkaline solutions, electrochemical impedance spectroscopy (EIS) and analyses were performed on a series of prepared materials. Nyquist curves for these materials are shown in Fig. 3g, and the measured data (scattered points) were fitted with Z-view software (solid line). Moreover, the equivalent circuit is shown, and the corresponding components are labeled in the illustration. Since the electrochemical impedances of all materials were tested in 0.1 M KOH solutions, the values of the solution resistance R_s were essentially the same, approximately 8.5 Ω cm^{-2}. Table S4 shows that $N_1S_1@CF$ exhibited the smallest R_c and R_t values among all samples, 11.98 and 109.7 Ω cm^{-2}, respectively, which indicated that the proper contents of N and S in the carbon framework were important in improving the electrochemical conductivity of the catalyst and that the collapse of the porous structure and reduction of the specific surface area caused by excessive doping tended to increase interfacial charge transfer resistance[32].

Stability is an important factor for practical application of an electrocatalyst; this is indicated in Fig. 3h, where the ORR stability of $N_1S_1@CF$ was tested with a RRDE, evaluated with a typical accelerated aging test, and compared with the performance of commercial Pt/C. After 5000 consecutive cycles of testing in an oxygen-saturated 0.1 M KOH solution, the results proved that the LSV curve half-wave potential of $N_1S_1@CF$ was reduced by only 9 mV, while that of commercial Pt/C was reduced by 38 mV. In addition, we also evaluated the stability of the catalyst by timing the current test. Figure 3i shows clearly that the current for Pt/C rapidly decreased to 72%. In contrast, $N_1S_1@CF$ maintained 97.4% of its initial current. Both measurements indicated that $N_1S_1@CF$ had better stability than Pt/C and showed potential for practical application[33].
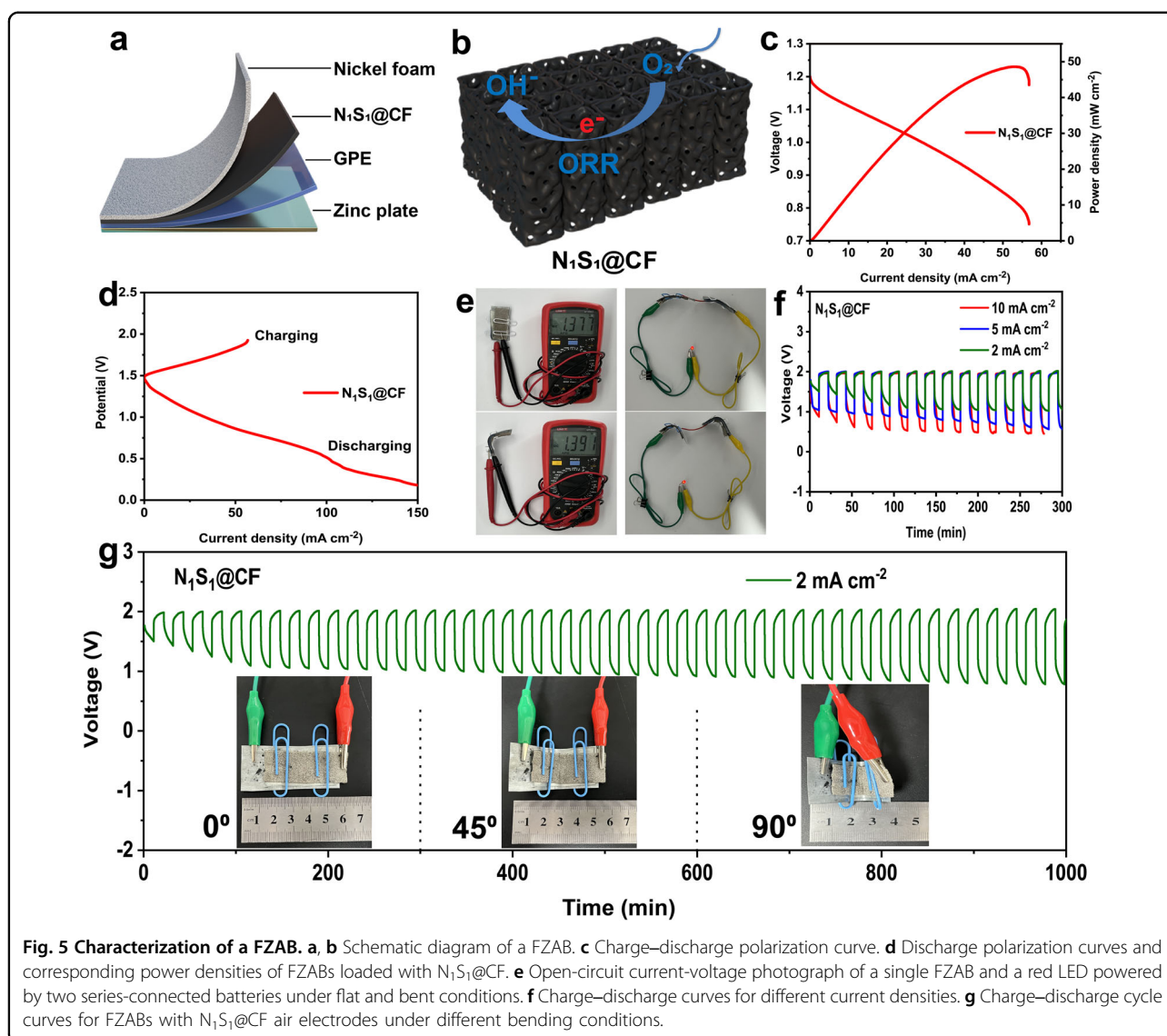
Because of the excellent ORR electrochemical performance and stability of the $N_1S_1@CF$ catalyst, we used it as a positive electrode catalyst for a ZAB. We assembled a primary ZAB for laboratory use, as indicated in Fig. 4a, by using carbon paper loaded with the $N_1S_1@CF$ catalyst as the air electrode, a zinc sheet as the negative electrode, and 6.0 M KOH containing 0.2 M $Zn(CH_3COO)_2$ as the electrolyte. In Fig. 4b, the charge/discharge polarization curves of ZABs based on $N_1S_1@CF$ showed low charge/discharge voltage gaps, indicating good charge/discharge capability. Figure 4c shows the polarization curves and power density curves of a ZAB with a peak power density of 221 mW cm^{-2} for $N_1S_1@CF$, which was larger than that of commercial Pt/C (138 mW cm^{-2}). The continuous discharge curves for $N_1S_1@CF$ and commercial Pt/C-based ZABs at different current densities are shown in Fig. 4d, and their voltage plateaus both decreased with increasing current density. As the current density was increased from 2 mA cm^{-2} to 50 mA cm^{-2}, all of the discharge voltages remained stable and smooth, and when the current density returned to the low discharge current density, the discharge voltages recovered to their original levels; this indicated that these ZABs showed good multiplicative performance, and this variation trend was basically consistent with the voltage variation trend of Pt/C. In addition, the mass-to-capacity was obtained by dividing the discharge capacity by the mass of zinc consumed during the test[34]. As indicated in Fig. 4e, the mass-specific capacity of $N_1S_1@CF$-based ZABs at a current density of 10 mA cm^{-2} was 792 mAh g$_{Zn}^{-1}$, which was larger than the specific capacities seen with current densities of 20 and 50 mA cm^{-2}. Furthermore, the EIS data of the ZABs displayed a relatively small charge transfer resistance of approximately 9 Ω, as shown in Fig. S12, which clearly demonstrated excellent charge transfer through the $N_1S_1@CF$ cathode[35]. To further examine stability, as indicated in Fig. 4f, the $N_1S_1@CF$ and Pt/C-based ZABs were charged and discharged at 20 mA cm^{-2} repeatedly, and the potential difference between the charging and discharging plateaus of the $N_1S_1@CF$-based ZABs changed very little after 100 h,

Fig. 4 Characterization of ZABs. a Schematic diagram of a ZAB. **b** Charge–discharge polarization curves. **c** Polarization curves and power densities of ZABs loaded with $N_1S_1@CF$ and commercial Pt/C. **d** Constant current discharge curves at different current densities for ZABs with $N_1S_1@CF$ as the cathode catalyst. **e** Mass-to-capacity curves. **f** Constant current discharge–charge cycle curves at 10 mA cm^{-2} for rechargeable ZABs with $N_1S_1@CF$ and commercial Pt/C as catalysts. **g** Constant current discharge–charge cycle curves at different current densities for ZABs. **h** Constant current discharge–charge cycle curves at 10 mA cm^{-2} for ZABs with $N_1S_1@CF$ as the catalyst, with the inset showing a homemade ZAB with a multimeter (left) and a white LED (∼3 V) powered by two integrated ZABs (right).

unlike that of Pt/C. Similarly, we also compared charge/discharge cycles of the ZABs at different current densities; as shown in Fig. 4g, the $N_1S_1@CF$-based ZABs also exhibited excellent stability when the current density was increased to 10 and 20 mA cm^{-2}. Moreover, as demonstrated in Fig. 4h, the charge–discharge stability of the battery was tested at a current density of 10 mA cm^{-2}. Figure S13 shows that the potential differences for the charge–discharge plateaus of the $N_1S_1@CF$-based ZABs were maintained at 0.9–0.95 V even after more than 230 h. The above analysis shows that the powdered nature of $N_1S_1@CF$ enabled successful application with liquid ZABs.

With the increasing demand for flexible wearable electronic devices, all-solid-state ZABs are emerging as useful energy devices promising environmental friendliness, power efficiency, and sustainability. The unique advantages

of the high electrocatalytic activity and high flexibility of the N, S-codoped carbon framework make it a candidate for use in rechargeable FZABs. As shown in Fig. 5a, FZABs were fabricated by using polished zinc sheets as the anodes, $N_1S_1@CF$ as the air cathodes, and polyvinyl alcohol (PVA) gel containing KOH as the gel polyvinyl alcohol electrolyte (GPE)[25]. Figure 5b shows that the microporous channels of $N_1S_1@CF$ promoted diffusion of oxygen and the electrolyte during the electrochemical reaction. The charge/discharge polarization curves and discharge power density curves for the FZABs are shown in Fig. 5c and d, respectively. The charge/discharge voltage gap of the FZAB was relatively small, and the maximum power density of the FZAB was 49 mW cm^{-2}. As indicated in Fig. 5e, a single FZAB provided a stable open-circuit potential of 1.37 V in ambient air in both the flat and bent states, and two FZABs connected in series easily powered a light-emitting diode (LED,

Fig. 5 Characterization of a FZAB. a, b Schematic diagram of a FZAB. **c** Charge–discharge polarization curve. **d** Discharge polarization curves and corresponding power densities of FZABs loaded with N_1S_1@CF. **e** Open-circuit current-voltage photograph of a single FZAB and a red LED powered by two series-connected batteries under flat and bent conditions. **f** Charge–discharge curves for different current densities. **g** Charge–discharge cycle curves for FZABs with N_1S_1@CF air electrodes under different bending conditions.

2.5 V) and demonstrated excellent voltage stability. Figure 5f shows the charge and discharge curves at different current densities for FZABs made with N_1S_1@CF. It is rather obvious that the FZABs exhibited smooth charging and discharging voltage plateaus at a current density of $2\,mA\,cm^{-2}$. Similarly, when the current density was increased to 5 and $10\,mA\,cm^{-2}$, the charging and discharging voltage plateaus of the FZABs remained smooth[36]. In addition, in evaluating the stability of the FZABs, as indicated in Fig. 5g, the charge–discharge potential differences seen with different bending levels for FZABs made with N_1S_1@CF did not change significantly at a current density of $2\,mA\,cm^{-2}$ and still displayed excellent charge–discharge cycling stability, which indicated outstanding flexibility. This result demonstrated the excellent charge–discharge performance of N_1S_1@CF in a FZAB and its feasibility for use in wearable electronic devices[37].

To gain insight into the excellent catalytic activity of N_1S_1@CF for oxygen reduction, we performed density functional theory (DFT) calculations to determine the roles of different functional groups on the defect edges of graphitic carbon during the oxygen reaction. Here, we constructed and calculated the following five models: graphite-nitrogen-doped graphene (Graphite-N@C), pyridine-nitrogen-doped graphene (Pyridine-N@C), pyrrole-nitrogen-doped graphene (Pyrrole-N@C), thiophene-sulfur-doped graphene (Thiophene-S@C), and a combination of the four commodified graphenes (N_1S_1@CF), as shown in Fig. 6a–e, respectively[38]. In addition, as illustrated in Fig. 6h, in an alkaline electrolyte solution, reduction of molecular oxygen requires 4 electrons and produces various intermediates, so it is usually called the "4-electron reaction pathway". As demonstrated in Fig. 6f, the Gibbs free energy for adsorption was calculated for different ORR intermediates with the five catalyst models, in
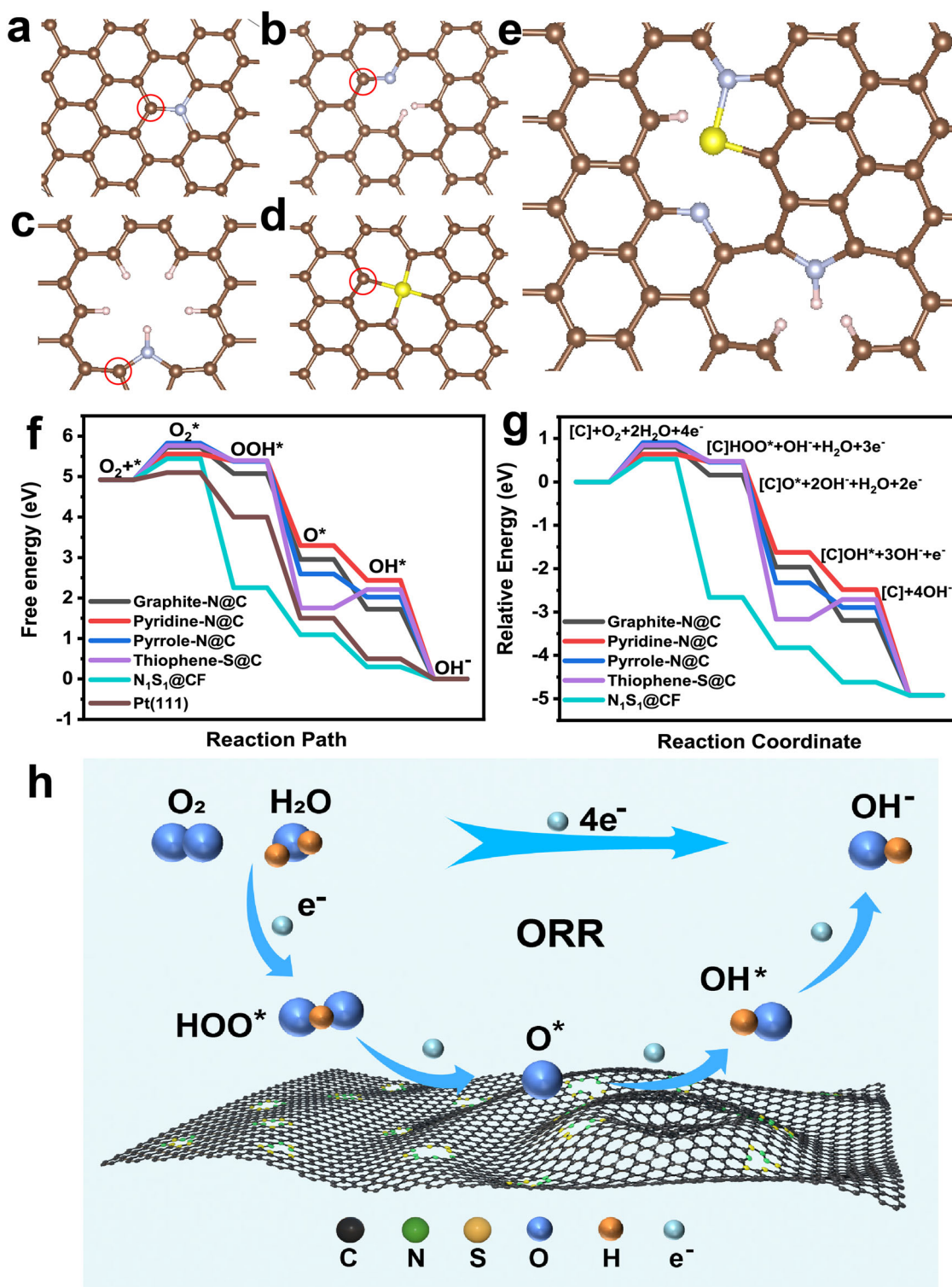
Fig. 6 Density functional theory calculations and analysis of N_1S_1@CF. Schematic structures of **a** graphite-N@C, **b** pyridine-N@C, **c** pyrrole-N@C, **d** thiophene-S@C, and **e** N_1S_1@C with the active sites used for the calculations marked by red circles, and ORR Gibbs free energies (**f**) and relative energies (**g**) are indicated. **h** Schematic representation of the electron transfer pathway for the ORR.

particular for the intermediates OOH*, O*, and OH*. For comparison, the adsorption energies of the ORR intermediates on Pt (111) were also calculated with the same conditions. Among the four models, the adsorption energies for OOH*, O*, and OH* intermediates on N_1S_1@CF were all lower than those for Pt (111), indicating that N_1S_1@CF had the best catalytic activity[39]. Figure 6g shows a plot of the relative energies for the ORR steps. For each reaction in these models, the corresponding energy decreased, and from a thermodynamic point of view, all basic steps proceeded spontaneously at zero potential with respect to the RHE ($U_{RHE} = 0$ V) since all of the electron transfer steps were exergonic ($\Delta G < 0$). It is evident that the energy reduction for N_1S_1@CF was the largest, further confirming that completion of the whole ORR process was more beneficial with N_1S_1@CF[40] and resulted in better ORR performance.

Conclusions

In summary, a simple method involving directional freezing and high-temperature pyrolysis was utilized to prepare N, S-doped porous carbon frameworks. By tuning the optimal N and S doping defect levels, adsorption of oxygen and its intermediates on the catalyst and the oxygen reduction reaction were promoted to enable the best ORR catalytic activity. When N_1S_1@CF was used as the electrode in an aqueous ZAB, it exhibited a high power density, high specific capacitance, and long-term cycling stability, which were better than those of most ZABs used for the ORR. In addition, due to its excellent mechanical flexibility and high electrochemical activity, N_1S_1@CF can be used as electrodes for all solid-state ZABs and provide great bendability and stable battery performance. This work provides a method with which to prepare an integrated flexible electrode with high-efficiency ORR electrocatalytic activity and expands the design strategies for flexible air electrodes and applications in flexible wearable devices.

Author details
[1]National Supercomputer Research Center of Advanced Materials, Advanced Materials Institute, Qilu University of Technology (Shandong Academy of Sciences), Jinan 250014, P. R. China. [2]Department of Chemistry, Shanghai Key Lab of Molecular Catalysis and Innovative Materials iChEM, Fudan University, Shanghai 200433, P. R. China. [3]ARC Research Hub for Computational Particle Technology, Monash University, Melbourne 3000, Australia. [4]School of Chemical Engineering and Graduate School of Biomedical Engineering, The University of New South Wales, Sydney 2052, Australia. [5]Yiwu Research Institute of Fudan University, Yiwu, Zhejiang 322000, P. R. China

Author contributions
H.P.P., M.W., and B.K. conceived the project and designed the experiments. H.P.P. and M.W. carried out the materials syntheses, characterizations, and electrochemical measurements. H.P.P. and P.P.S. wrote the paper. All authors discussed the results and commented on the manuscript. The manuscript was based on the contributions of all authors. All authors have agreed to the final version of the manuscript.

Conflict of interest
The authors declare no competing interests.

References
1. He, B. et al. Superassembly of porous Fe$_{tet}$(NiFe)$_{oct}$O frameworks with stable octahedron and multistage structure for superior lithium–oxygen batteries. *Adv. Energy Mater.* **10**, 1904262 (2022).
2. Zhang, H. et al. Ultrastable FeCo bifunctional electrocatalyst on Se-doped CNTs for liquid and flexible all-solid-state rechargeable Zn-air batteries. *Nano. Lett.* **21**, 2255–2264 (2021).
3. Zhang, R. et al. Super-assembled hierarchical CoO nanosheets-Cu foam composites as multi-level hosts for high-performance lithium metal anodes. *Small* **17**, e2101301 (2021).
4. Zhang, R. et al. Atomic layer deposition assisted superassembly of ultrathin ZnO layer decorated hierarchical Cu foam for stable lithium metal anode. *Energy Storage Mater.* **37**, 123–134 (2021).
5. Zhou, T. et al. Ultrathin cobalt oxide layers as electrocatalysts for high-performance flexible Zn-air batteries. *Adv. Mater.* **31**, e1807468 (2019).
6. Chen, S. et al. Nanostructured polyaniline-decorated Pt/C@PANI core-shell catalyst with enhanced durability and activity. *J. Am. Chem. Soc.* **134**, 13252–13255 (2012).
7. Gong, H. et al. Ni$_3$Fe nanoalloys embedded in N-doped carbon derived from dual-metal ZIF: efficient bifunctional electrocatalyst for Zn-air battery. *Carbon* **174**, 475–483 (2021).
8. Lyu, D. et al. Carbon matrix-encapsulated Co$_9$S$_8$ nanoparticles as a highly efficient and durable bifunctional oxygen redox electrocatalyst for rechargeable Zn–air batteries. *Adv. Energy Mater.* **11**, 2101249 (2021).
9. Lee, D., Kim, H. W., Kim, J. M., Kim, K. H. & Lee, S. Y. Flexible/rechargeable Zn-air batteries based on multifunctional heteronanomat architecture. *ACS Appl. Mater. Inter.* **10**, 22210–22217 (2018).
10. Wang, Y., Cao, Q., Guan, C. & Cheng, C. Recent advances on self-supported arrayed bifunctional oxygen electrocatalysts for flexible solid-state Zn-air batteries. *Small* **16**, e2002902 (2020).
11. Niu, Q. et al. Flexible, porous, and metal-heteroatom-doped carbon nanofibers as efficient ORR electrocatalysts for Zn-air battery. *Nano. Lett.* **11**, 8 (2019).
12. Chen, P. et al. Recent progress in electrolytes for Zn-air batteries. *Front. Chem.* **8**, 372 (2020).
13. Chen, Y. et al. Enhanced oxygen reduction with single-atomic-site iron catalysts for a zinc-air battery and hydrogen-air fuel cell. *Nat. Commun.* **9**, 5422 (2018).
14. Pei, Z. et al. Texturing in situ: N,S-enriched hierarchically porous carbon as a highly active reversible oxygen electrocatalyst. *Energy Environ. Sci.* **10**, 742–749 (2017).
15. Sun, T. et al. B, N codoped and defect-rich nanocarbon material as a metal-free bifunctional electrocatalyst for oxygen reduction and evolution reactions. *Adv. Sci.* **5**, 1800036 (2018).
16. Wang, C. et al. A directional strain sensor based on anisotropic micro-honeycomb cellulose nanofiber-carbon nanotube hybrid aerogels prepared by unidirectional freeze drying. *Small* **15**, e1805363 (2019).
17. Zheng, Q., Cai, Z., Ma, Z. & Gong, S. Cellulose nanofibril/reduced graphene oxide/carbon nanotube hybrid aerogels for highly flexible and all-solid-state supercapacitors. *Acs. Appl. Mater. Inter.* **7**, 3263–3271 (2015).
18. Barrios, E. et al. Nanomaterials in advanced, high-performance aerogel composites: a review. *Polymers* **11**, 726 (2019).

19. Wang, M., Shao, C., Zhou, S., Yang, J. & Xu, F. Super-compressible, fatigue resistant and anisotropic carbon aerogels for piezoresistive sensors. *Cellulose* **25**, 7329–7340 (2018).

20. Liang, X. et al. Highly compressible carbon sponge supercapacitor electrode with enhanced performance by growing nickel-cobalt sulfide nanosheets. *Acs. Appl. Mater. Inter.* **10**, 10087–10095 (2018).

21. Chen, C. et al. Scalable and sustainable approach toward highly compressible, anisotropic, lamellar carbon sponge. *Chem* **4**, 544–554 (2018).

22. Hao, P. et al. Hierarchical porous carbon aerogel derived from bagasse for high performance supercapacitor electrode. *Nanoscale* **6**, 12120–12129 (2014).

23. Zhu, J. et al. Defective N/S-codoped 3D cheese-like porous carbon nanomaterial toward efficient oxygen reduction and Zn-air batteries. *Small* **14**, e1800563 (2018).

24. Ye, T. N., Lv, L. B., Li, X. H., Xu, M. & Chen, J. S. Strongly veined carbon nanoleaves as a highly efficient metal-free electrocatalyst. *Angew. Chem. Int. Ed.* **53**, 6905–6909 (2014).

25. Liu, P. et al. Bifunctional oxygen electrocatalyst of mesoporous Ni/NiO nanosheets for flexible rechargeable Zn-air batteries. *Nano. Lett.* **12**, 68 (2020).

26. Chen, B. et al. MO-Co@N-doped carbon (M = Zn or Co): vital roles of inactive Zn and highly efficient activity toward oxygen reduction/evolution reactions for rechargeable Zn-air battery. *Adv. Funct. Mater.* **27**, 1700795 (2017).

27. Chen, Y. et al. Hydrophobic 3D Fe/N/S doped graphene network as oxygen electrocatalyst to achieve unique performance of zinc-air battery. *Chem. Eng. J.* **353**, 472–480 (2018).

28. Tao, X. et al. Balancing surface adsorption and diffusion of lithium-polysulfides on nonconductive oxides for lithium-sulfur battery design. *Nat. Commun.* **7**, 11203 (2016).

29. Fang, W. et al. Fe$_{0.96}$S/Co$_8$FeS$_8$ nanoparticles co-embedded in porous N, S codoped carbon with enhanced bifunctional electrocatalystic activities for all-solid-state Zn-air batteries. *Appl. Sur. Sci.* **505**, 144212 (2020).

30. Han, J. et al. Single-atom Fe-Nx-C as an efficient electrocatalyst for zinc–air batteries. *Adv. Funct. Mater.* **29**, 1808872 (2019).

31. Huang, L. B. et al. Engineering carbon-shells of M@NC bifunctional oxygen electrocatalyst towards stable aqueous rechargeable Zn-air batteries. *Chem. Eng. J.* **418**, 129409 (2021).

32. Li, S., Cheng, C., Zhao, X., Schmidt, J. & Thomas, A. Active salt/silica-templated 2D mesoporous FeCo-Nx-carbon as bifunctional oxygen electrodes for zinc-air batteries. *Angew. Chem. Int. Ed.* **57**, 1856–1862 (2018).

33. Li, J. et al. Well-dispersed ultrafine CoFe nanoalloy decorated N-doped hollow carbon microspheres for rechargeable/flexible Zn-air batteries. *Chem. Eng. J.* **407**, 127961 (2021).

34. Liu, W. et al. Controllable urchin-like NiCo$_2$S$_4$ microsphere synergized with sulfur-doped graphene as bifunctional catalyst for superior rechargeable Zn-air battery. *Adv. Funct. Mater.* **28**, 1706675 (2018).

35. Lu, Q. et al. Tailoring charge and mass transport in cation/anion-codoped Ni$_3$N/N-doped CNT integrated electrode toward rapid oxygen evolution for fast-charging zinc-air batteries. *Energy Storage Mater.* **39**, 11–20 (2021).

36. Xu, Q. et al. In-situ enriching active sites on co-doped Fe-Co$_4$N@N-C nanosheet array as air cathode for flexible rechargeable Zn-air batteries. *Appl. Cata. B.* **256**, 117893 (2019).

37. Su, C.-Y. et al. Atomic modulation of FeCo-nitrogen-carbon bifunctional oxygen electrodes for rechargeable and flexible all-solid-state zinc-air battery. *Adv. Energy Mater.* **7**, 1602420 (2017).

38. Yuan, H. et al. Facilitation of sulfur evolution reaction by pyridinic nitrogen doped carbon nanoflakes for highly-stable lithium-sulfur batteries. *Energy Storage Mater.* **10**, 1–9 (2018).

39. Xu, H., Cheng, D., Cao, D. & Zeng, X. C. A universal principle for a rational design of single-atom electrocatalysts. *Nat. Cata.* **1**, 339–348 (2018).

40. Li, Y. et al. A self-sponsored doping approach for controllable synthesis of S and N co-doped trimodal-porous structured graphitic carbon electrocatalysts. *Energy Environ. Sci.* **7**, 3720–3726 (2014).